Mon. Not. R. Astron. Soc. **359,** 16–30 (2005) doi:10.1111/j.1365-2966.2005.08696.x

Very Small Array observations of the Sunyaev–Zel'dovich effect in nearby galaxy clusters

Katy Lancaster,[1*†] Ricardo Genova-Santos,[2] Nelson Falcón,[2,3] Keith Grainge,[1]
Carlos Gutiérrez,[2] Rüdiger Kneissl,[1] Phil Marshall,[4] Guy Pooley,[1] Rafael Rebolo,[2,5]
Jose-Alberto Rubiño-Martin,[2] Richard D. E. Saunders,[1] Elizabeth Waldram[1]
and Robert A. Watson[6]

[1]*Astrophysics Group, Cavendish Laboratory, University of Cambridge, Madingley Road, Cambridge CB3 0HE*
[2]*Instituto de Astrofisíca de Canarias, 38200 La Laguna, Tenerife, Canary Islands, Spain*
[3]*Dpt. de Fisica, FACYT, Universidad de Carabobo, Venezuela*
[4]*Kavli Institute for Particle Astrophysics and Cosmology, Stanford University, PO Box 20450, MS29, Stanford, CA 94309, USA*
[5]*Consejo Superior de Investigaciones Cientificas, Calle Serrano 117, 28006 Madrid, Spain*
[6]*Jodrell Bank Observatory, University of Manchester, Macclesfield, Cheshire SK11 9DL*

Accepted 2004 December 1. Received 2004 October 27; in original form 2004 May 28

ABSTRACT

We present Very Small Array (VSA) observations (centred on ≈34 GHz) on scales ≈20 arcmin towards a complete, X-ray flux-limited sample of seven clusters at redshift $z < 0.1$. Four of the clusters have significant Sunyaev–Zel'dovich (SZ) detections in the presence of cosmic microwave background (CMB) primordial anisotropy. For all seven, we use a Bayesian Markov Chain Monte Carlo (MCMC) method for inference from the VSA data, with X-ray priors on cluster positions and temperatures, and radio priors on sources. In this context, the CMB primordial fluctuations are an additional source of Gaussian noise, and are included in the model as a non-diagonal covariance matrix derived from the known angular power spectrum. In addition, we make assumptions of β-model gas distributions and of hydrostatic equilibrium, to evaluate probability densities for the gas mass ($M_{\rm gas}$) and total mass ($M_{\rm r}$) out to r_{200}, the radius at which the average density enclosed is 200 times the critical density at the redshift of the cluster. This is further than has been done before and close to the classical value for a collapsed cluster. Our combined estimate of the gas fraction ($f_{\rm gas} = M_{\rm gas}/M_{\rm r}$) is $0.08^{+0.06}_{-0.04}\,h^{-1}$. The random errors are poor (note, however, that the errors are higher than would have been obtained with the usual χ^2 method on the same data) but the control of bias is good. We have described the MCMC analysis method specifically in terms of SZ but hope the description will be of more general use. We find that the effects of primordial CMB contamination tend to be similar in the estimates of both $M_{\rm gas}$ and $M_{\rm r}$ over the narrow range of angular scales we are dealing with, so that there is little effect of primordials on $f_{\rm gas}$ determination. Using our $M_{\rm r}$ estimates we find a normalization of the mass–temperature relation based on the profiles from the VSA cluster pressure maps, which is in good agreement with recent *M*–*T* determinations from X-ray cluster measurements.

Key words: galaxies: clusters: general – cosmic microwave background – cosmology: observations – X-rays: galaxies: clusters.

1 INTRODUCTION

Galaxy clusters have long been thought to provide a faithful sample of cosmic baryonic matter (see, for example, White et al. 1993; Evrard 1997). One quantity often calculated and assessed in such work is the gas fraction $f_{\rm gas}$, which is defined as the (baryonic) gas mass over the total (baryonic plus dark matter) mass of the cluster.

---

[*] E-mail: katy.lancaster@bristol.ac.uk

[†] Present address: Physics Department, University of Bristol, Tyndall Avenue, Bristol BS8 1TL.

We here present Sunyaev–Zel'dovich (SZ; Sunyaev & Zel'dovich 1972; see also, for example, Birkinshaw 1999; Carlstrom, Holder & Reese 2002) observations of a sample of clusters, from which we infer $f_{\rm gas}$. Our random errors are high but the sample is complete, the redshifts deliberately low, and we are able to estimate $f_{\rm gas}$ out to radii at which the overdensity of the enclosed region is close to the classical value of 178 for a collapsed object (see, for example, Peacock 1999). First we review some of the existing $f_{\rm gas}$ measurements.

A popular route in investigating cosmic baryonic matter is the detailed study of the X-ray emission from cluster gas. For example, in an investigation based on *ROSAT* Position Sensitive Proportional Counter (PSPC) data (Ettori & Fabian 1999), a sample of 36 clusters of redshift $0.05 \leqslant z \leqslant 0.44$ was used to measure $f_{\rm gas}$. Assumptions of isothermality and hydrostatic equilibrium were required. The resulting $f_{\rm gas}$ distribution (within r_{500}; that is, where the mean density inside this radius is 500 times the critical density at the redshifts of the clusters) was centred on a value $f_{\rm gas}(r_{500}) = 0.168\, h_{50}^{-1.5}$. Values for individual clusters were found to vary between 0.101 and 0.245. Mohr, Mathiesen & Evrard (1999) also analysed PSPC data on 45 X-ray selected clusters, finding a mean $f_{\rm gas}(r_{500})$ of $0.212\, h_{50}^{-1.5}$ in a subsample of 27 clusters hotter than 5 keV. Following a similar route (supplemented by gravitational lensing information on the total mass) with *Chandra* imaging spectrometer data, Allen, Schmidt & Fabian (2002) find, for a set of six clusters with $0.103 \leqslant z \leqslant 0.461$, a mean $f_{\rm gas}$ within r_{2500} of $0.113 \pm 0.005\, h_{70}^{-1.5}$ for a Λ cold dark matter (CDM) model, a very precise determination with very similar values for each cluster. With additional data, Allen et al. (2003) investigated the observed change of $f_{\rm gas}$ with cosmology.

Studies making use of the SZ effect have potential advantages for gas and gravitational potential measurements (where the potential is obtained via calculation of the total mass). The X-ray signal is proportional to $n_{\rm e}^2$ (where $n_{\rm e}$ is electron density), while the SZ signal is proportional to $n_{\rm e}$. This means that SZ is less biased to concentration and can constrain clumping. Although X-ray telescopes achieve excellent signal-to-noise, they are restricted to observing the denser, inner regions of a cluster (e.g. out to r_{2500}). With SZ, it is possible to measure $n_{\rm e}(r)$ over a larger range of r (e.g. close to the virial radius) as less dynamic range is required.

Myers et al. (1997) used the Owens Valley Radio Observatory (OVRO) 5.5-m telescope to observe the SZ effect in three clusters at 32 GHz. With the addition of the Coma cluster (observed by Herbig et al. 1995), they obtain a gas fraction of $f_{\rm gas} = 0.061 \pm 0.011\, h_{100}^{-1}$. This sample of objects lies in the redshift range $0.023 \leqslant z \leqslant 0.0899$, and includes three clusters, which we also present here. [Mason, Myers & Readhead (2001) extend the sample to seven clusters, incorporating a further two discussed in this paper. The data were used to calculate H_0.]

Grego et al. (2001) used the OVRO and Berkeley–Illinois–Maryland Association (BIMA) arrays to make SZ observations of galaxy clusters at 30 GHz. The data were used to infer the gas mass and total mass, thus constraining $f_{\rm g}$ (within r_{500}) in 18 X-ray selected clusters in the redshift range $0.171 \leqslant z \leqslant 0.826$. The mean value obtained for the full sample was $f_{\rm gas} = 0.081^{+0.009}_{-0.011}\, h_{100}^{-1}$. In addition, a 'fair' subsample is defined as the five most X-ray luminous clusters in the EMSS sample. These objects have redshift $0.328 \leqslant z \leqslant 0.826$, and together give a mean gas fraction $f_{\rm gas} = 0.089^{+0.018}_{-0.019}\, h_{100}^{-1}$.

One of the aims of the Very Small Array (VSA) project (Watson et al. 2003; Taylor et al. 2003; Scott et al. 2003; Rubiño-Martin et al. 2003; Grainge et al. 2003; Slosar et al. 2003; Dickinson et al. 2004; Rebolo et al. 2004) has been to image nearby, massive clusters in SZ. The VSA baselines at ≈34 GHz couple well to the angular scales of such clusters. Here we describe SZ observations and cluster-parameter inferences of an X-ray selected, complete sample of seven clusters, with redshift $0.023 \leqslant z \leqslant 0.098$ and median 0.075. The age of the Universe at $z = 0.075$ is 1.7 times its age at $z = 0.55$. The importance of low-z work is illustrated by the following two points.

(i) The low redshifts of the clusters mean that they have particularly good X-ray data, and one can be reasonably confident that bright X-ray selected complete samples are in fact complete.

(ii) Because clusters grow under gravity, then on average low-redshift clusters should be more evolved than those at higher redshift. Comparison of, for example, $f_{\rm gas}$ in low- and high-z samples is important. (Of course, we do not know how big the samples have to be to encompass meaningful averages.)

One immediate difficulty on these angular scales is contamination by cosmic microwave background (CMB) primordial anisotropy. At the start of this VSA observational programme, it was evident that we needed an analysis method that would apply the inference process correctly and would properly cope with error distributions in low signal-to-noise situations. There is the additional difficulty of dealing with (potentially variable) radio sources at 34 GHz. This could be especially problematic where sources are in the clusters themselves rather than in the background; the low redshifts of the clusters imply such sources may be very bright. Accounting for these effects correctly necessitates the exploration of the posterior probabilities of the parameters of a β-model for the gas distribution given the VSA visibilities, receiver noise, the CMB and radio sources. The method must also incorporate prior knowledge on, for example, the cluster positions from X-rays, and on source fluxes in a way which can cope with variability. We assume isothermality, and that the clusters are well described by hydrostatic equilibrium. We use a Markov Chain Monte Carlo (MCMC) sampler (BAYESYS) for an acceptable combination of speed and accuracy.

In Section 2 we briefly describe the relevant features of the VSA. In Section 3 we present the sample, outline the data reduction pipeline and describe our strategy for dealing with radio sources. In Section 4 we present our results, and attempt to describe the Bayesian analysis method in non-specialist terms. We make concluding comments in Section 5.

2 VERY SMALL ARRAY

The VSA is a 14-element interferometric telescope situated at the Observatorio del Teide, Tenerife. The observing frequency is tunable in the 26–36 GHz range, with a bandwidth of 1.5 GHz; at these frequencies observations should be relatively free from contamination by Galactic foregrounds for fields at high Galactic latitude. The 14 antennas are identical. They rotate independently and are mounted on a tilting table, thus allowing tracking in two dimensions. The table is surrounded by an aluminium shield to prevent groundspill.

The telescope was designed to operate in two configurations: compact (see, for example, Watson et al. 2003 for technical details) and extended (see Grainge et al. 2003). All data in this paper were taken using the extended configuration. The Extended Array has 322-mm diameter illuminated apertures, resulting in a primary beam of 2°.0 FWHM when operating at 34 GHz. The horn arrangement on the table allows for a range of baselines between approximately 40 cm and 3 m. The telescope is sensitive to angular sizes in the range $0^\circ.25 < \theta < 1^\circ.2$, and is ideal for observing low-redshift clusters.

Radio sources are a problem in all cm-wave CMB observations at all but the lowest angular resolutions, and SZ is no exception. The VSA design includes a dedicated source-subtraction telescope. This comprises two 3.7-m dishes located next to the main array and used as an interferometer with a 9-m baseline, giving 4-arcmin resolution and a 9-arcmin field of view. The source-subtractor does not resolve any of the sources which we observe, but resolves out the CMB fluctuations.

3 OBSERVATIONS

3.1 Galaxy clusters

The VSA targets were selected from the Northern *ROSAT* All-Sky Survey (NORAS; Böhringer et al. 2000) as the seven most X-ray luminous objects at redshift <0.1. The clusters have rest-frame X-ray luminosity $>5 \times 10^{37}$ W in the 0.1–2.4 keV energy band. Additionally, only clusters observable from Tenerife and Cambridge were considered. This imposed declination limits of $10^\circ < \delta < 60^\circ$. The upper limit is set by the latitude and configuration of the VSA main array. The lower limit is set by the need to use the Ryle Telescope (RT) as part of the source-subtraction strategy (see Section 3.3). Note that we have not applied any criteria concerning fluxes of contaminant radio sources. This is unlike the VSA primordial work, and indeed the SZ work of the RT and OVRO/BIMA.

Pointing centres for the seven fields were defined based on the X-ray positions of the clusters as published in NORAS. Data for each target were obtained in a series of short observations made during the period 2001 October to 2003 August. Repeat observations were required in several cases due to uncharacteristically persistent bad weather. The sample is summarized in Table 1, along with published redshifts, temperatures used in our analysis, X-ray luminosities and total integration times of the VSA observations. The clusters A401 and A399 are only separated by around a degree, so were observed in a single pointing centred on A401.

3.2 Calibration and data reduction

The primary calibrator for all VSA observations is Jupiter. We based our calibration scale on the effective temperature of the planet at 34 GHz: $T_{34} = 155 \pm 5$ K (Mason et al. 1999). The flux scale is transferred to our other calibration sources: Cas A and Tau A. The calibrators are observed on a daily basis, allowing flux and phase calibration at regular intervals. Cas A and Tau A are partially resolved on the longest VSA observations; we overcome this problem by applying models as discussed in Grainge et al. (2003). Full details of the VSA calibration will be presented in a forthcoming paper. Note that in Dickinson et al. (2004) and Rebolo et al. (2004) we rescale our calibration to agree with the recent *Wilkinson Microwave Anisotropy Probe* (*WMAP*) results.

The data reduction pipeline for galaxy clusters is identical to that employed in the processing of our CMB data, and is presented in detail in Watson et al. (2003). Each observation is analysed independently using the REDUCE software, developed by the VSA team. The procedure is now highly developed, allowing virtually automatic correcting, flagging, filtering and reweighting of the data. However, each raw data file must be checked by eye at least once to eliminate some 'bad' data (due to bad weather or telescope malfunction), and to ensure optimum quality in the reduced data. It is also necessary to identify files requiring special filtering depending on where the Sun, Moon or a bright planet was during the observation. The resulting calibrated visibilities from each observation are taken and stacked together.

The data were reduced independently by the groups at the Cavendish, the Instituto de Astrofisíca de Canarias and Jodrell Bank Observatory, and the results were found to be fully consistent. Approximately 28 per cent of the data were discarded due to bad weather, filtering and telescope down-time.

The form of data from the single baseline source-subtraction interferometer is identical to that of the main array and is processed in a similar way. The primary flux calibrator is NGC 7027. The flux scale from this is applied to our other flux calibrators. We use interleaved calibrators in order to monitor the telescope phase.

3.3 Radio sources

Contamination by radio sources can be a large problem for CMB observations. The contribution goes as ℓ^2, and so tends to be more problematic for the (often higher-resolution) SZ work than for primordial CMB observations. In order to map the SZ effect accurately, it is necessary to account for the effect of radio sources which may be part of, in front of, or behind the cluster. The VSA source-subtraction interferometer allows potentially problematic sources to be observed simultaneously with main array observations of the cluster fields.

As no high-frequency ($\approx$34 GHz) survey of the radio sky is available, we scheduled source observations via a twofold approach, as follows.

(i) The National Radio Astronomy Observatory (NRAO) Very Large Array (VLA) Sky Survey (NVSS) and GB6 catalogues (Condon et al. 1998; Gregory et al. 1996) were examined for sources within a radius of 2° from the cluster centres. Source fluxes at 1.4 and 4.9 GHz were used to perform a simple extrapolation to 30 GHz, thus making some prediction of the approximate level of contamination in the SZ observations. All sources with predicted flux greater than 50 mJy were selected for observation with the VSA source-subtractor.

Table 1. The VSA cluster sample: cluster coordinates (Böhringer et al. 2000), redshift (Struble & Rood 1991), electron temperature (Markevitch et al. 1998), except Coma (Hughes, Gorenstein & Fabricant 1988), X-ray luminosity (Böhringer et al. 2000), integration time and map rms (outside the primary beam).

Cluster	RA (B1950)	Dec. (B1950)	z	T_e (keV)	L_X (10^{37} W)	T_{int} (h)	rms (Jy)
Coma	12 57 18.29	28 12 28.5	0.0232	9.1 ± 0.7	7.01	80	0.021
A1795	13 46 34.43	26 50 37.5	0.0616	7.8 ± 1.0	9.93	115	0.020
A399	02 55 05.33	12 50 57.6	0.0715	7.0 ± 0.4	6.78	96	0.030
A401	02 56 12.55	13 22 50.1	0.0748	8.0 ± 0.4	11.76	96	(As A399)
A478	04 10 40.89	10 20 26.0	0.0882	$8.4^{+0.8}_{-1.4}$	13.31	74	0.018
A2142	15 56 16.45	27 22 08.0	0.0899	$9.7^{+1.5}_{-1.1}$	20.52	73	0.023
A2244	17 00 52.86	34 07 54.5	0.0980	$7.1^{+5.0}_{-2.2}$	7.39	91	0.018

Table 2. Radio sources present in the cluster fields. The source marked with an asterisk was predicted to have flux less than 50 mJy, but Mason et al. (2001) suggest it may be variable.

	RA (B1950)	Dec. (B1950)	Predicted flux 34 GHz (mJy)	RT survey 15 GHz (mJy)	VSA source-subtractor 34 GHz (mJy)
Coma	12 48 36	+28 39 47	75		46 ± 11
	12 49 25	+28 07 55	71		29 ± 9
	12 50 49	+27 55 57	99		82 ± 8
	12 51 46	+27 53 41	311		250 ± 3
	12 54 04	+27 17 17	57		56 ± 5
	12 55 36	+28 36 36	96	49 ± 3	26 ± 9
	12 56 08	+29 25 19	53		10 ± 12
	12 57 11	+28 13 40	–	27 ± 3	34 ± 7
	12 58 04	+28 46 18	226	251 ± 13	207 ± 10
	12 58 56	+28 37 45	–	34 ± 3	31 ± 5
	12 58 59	+28 58 59	168		10 ± 7
	12 59 58	+27 25 17	58		49 ± 9
	13 03 59	+27 18 37	52		45 ± 9
A1795	13 39 50	+27 24 42	521		380 ± 9
	13 45 45	+25 16 01	521		12 ± 7
	13 46 09	+26 42 42	89		8 ± 10
	13 46 34	+26 50 25	36	51 ± 3	31 ± 9
	13 49 03	+27 19 48	–	8 ± 3	20 ± 11
	13 49 41	+25 24 17	71		7 ± 6
A399/A401	02 53 51	+13 22 25	325	342 ± 17	235 ± 8
	02 55 24	+13 40 10	32*		36 ± 4
	02 55 47	+13 22 19	37	52 ± 3	29 ± 4
	02 56 01	+11 31 00	84		54 ± 9
	02 56 52	+13 42 59	35	66 ± 3	26 ± 5
	02 57 25	+11 25 45	60		55 ± 4
	02 58 34	+13 03 53	28	17 ± 3	13 ± 6
	02 59 48	+12 07 18	305		107 ± 9
	03 00 23	+12 57 22	80		97 ± 7
A478	04 08 52	+08 35 38	190		61 ± 12
	04 10 55	+11 04 43	836		395 ± 9
	04 11 02	+10 10 19	–	14 ± 3	7 ± 4
A2142	15 48 08	+27 27 02	166		58 ± 7
	15 52 28	+27 55 35	61		2 ± 6
	15 58 04	+27 11 13	163		5 ± 6
	15 58 57	+26 53 35	–	56 ± 3	17 ± 6
	16 00 03	+26 18 43	57		38 ± 6
	16 00 35	+26 54 15	498		176 ± 14
	16 04 54	+27 25 22	326		186 ± 17
A2244	16 53 50	+32 48 55	88		48 ± 6
	16 56 12	+34 48 01	512		297 ± 11
	17 06 12	+33 50 37	110		95 ± 8

(ii) In order to account for flat or rising spectrum sources not seen at the lower frequencies, the RT was used to survey the central square degree of each field at 15 GHz with the rastering technique described by Waldram et al. (2003). Peaks $\gtrsim$20 mJy in the raster maps were recorded and the corresponding position list was added to the source-subtractor observing queue. This ensured that we accounted not only for all potentially bright sources in the field, but also for fainter sources which may have been present in the critical central regions of the SZ fields.

A summary of the source lists for all clusters is presented in Table 2, including fluxes measured by the source-subtractor. The 15-GHz fluxes are those from RT pointed observations. Whereas for our primordial anisotropy work source fluxes were subtracted directly from the visibilities, we choose here to use our measured fluxes as priors in the Bayesian fitting software. As a result of telescope malfunction at various stages during our observing schedule, not all sources were observed simultaneously with the corresponding cluster. In order to account for possible variability in the source flux, broader priors were used than would have been assumed otherwise. Directly subtracting source fluxes with such uncertainties would lead to biases when fitting to the SZ data.

We can assess how much the SZ detections are affected by confusion noise from sources not found in the above, as follows. A

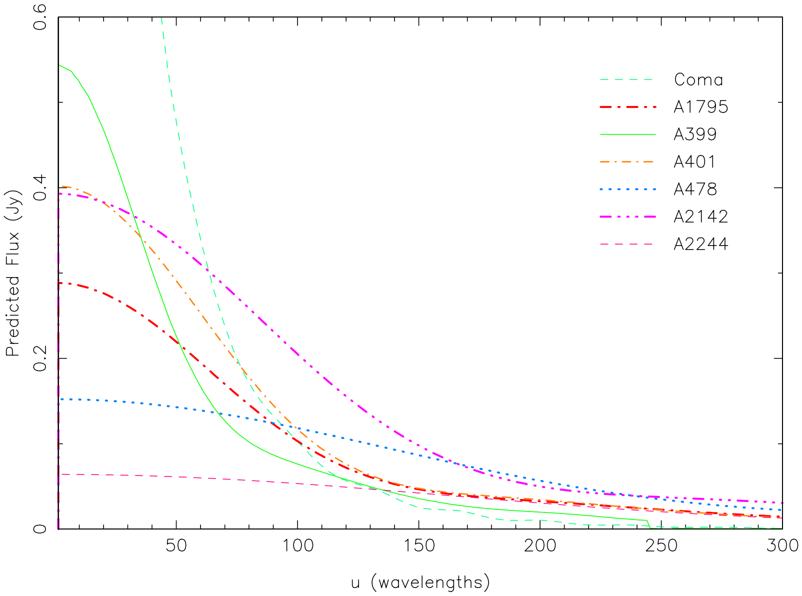

Figure 1. Predicted SZ profiles for the cluster sample.

corollary of the work of Scheuer (1957) is that confusion is worst when there is approximately one source per synthesized beam. Examination of Table 2 shows that in the RT surveying, at about 20 mJy there is less than one source per VSA average SZ synthesized beam. A rough extrapolation indicates that there is one source per beam at 34 GHz at a level of 10 mJy. Because the detected SZ fluxes are ≈150 mJy, it is evident that the source strategy is adequate.

4 RESULTS

4.1 Maps

The flagged and stacked data are held as visibility files, containing the real and imaginary parts for each observed *uv* position along with an associated rms noise level. Standard AIPS tasks are used to make maps, and to perform CLEANing using one CLEAN box encompassing the area of the VSA primary beam. All analysis and parameter fitting is performed in the visibility plane; the maps presented here along with the resulting discussion are included purely to illustrate the results of our SZ programme.

We expect a larger SZ response on the shortest baselines, so an appropriate Gaussian taper is applied in each case. This emphasizes structure on large scales. Taper values were chosen based on the range of *uv* radii available in each cluster's data. In order to determine appropriate tapers for our sample, we used cluster parameters from Mason et al. (2001) (as listed in Table 5) to generate predicted SZ profiles. These are shown in Fig. 1. [We observe that the Mason et al. (2001) value for the core radius of A399 (4.33 ± 0.45 arcmin) is in direct conflict with that reported by Sanderson & Ponman (2003) (1.89 ± 0.36 arcmin). The use of the Mason et al. parameter may result in an overestimate of the SZ flux from this cluster.] The chosen tapers are ≈0.1 kλ, although the taper for Coma would ideally be ≈0.023 kλ. This cuts out nearly all Extended Array baselines, so a value of ≈0.1 kλ was used with good results. These maps of the VSA cluster sample are presented in Fig. 2. The contours are 1.5σ, where σ is the rms noise level presented in Table 1. We comment on the significance of the detections in each map, and also the strength of the observed primordial features. We emphasize that this is not intended to be a quantitative analysis of the signal-to-noise ratio achieved for each cluster.

4.1.1 *Coma: map (a)*

Coma is at redshift $z = 0.0232$, giving it an angular size on the sky roughly four times greater than any other cluster in the sample. It would ideally be observed on baselines even shorter than those of the VSA. However, the SZ signal from this cluster is so strong, we detect it at 7.5σ. 4.5σ primordial features are visible around the SZ decrement.

4.1.2 *A1795: map (b)*

A1795 is also detected at the 7.5σ level. This map contains a bright positive primordial feature south of the cluster.

4.1.3 *A399 and A401: map (c)*

A399 does not appear in the map. We argue that this is most probably due to contamination by primordial CMB. Although the contours are negative at the position of A401, we suggest that this is largely due to the primordial decrement east of the cluster position. The SZ signal from the cluster may be contributing in part, but it is important not to confuse the two effects. The centre of the obvious decrement is around 15 arcmin away from the X-ray centre of A401.

4.1.4 *A478: map (d)*

The A478 map shows a 6σ SZ detection. Primordial CMB structures are visible all around the cluster, varying in strength from 3σ to 4.5σ.

4.1.5 *A2142: map (e)*

The 7.5σ detection of A2142 appears to be relatively free from bright primordial features.

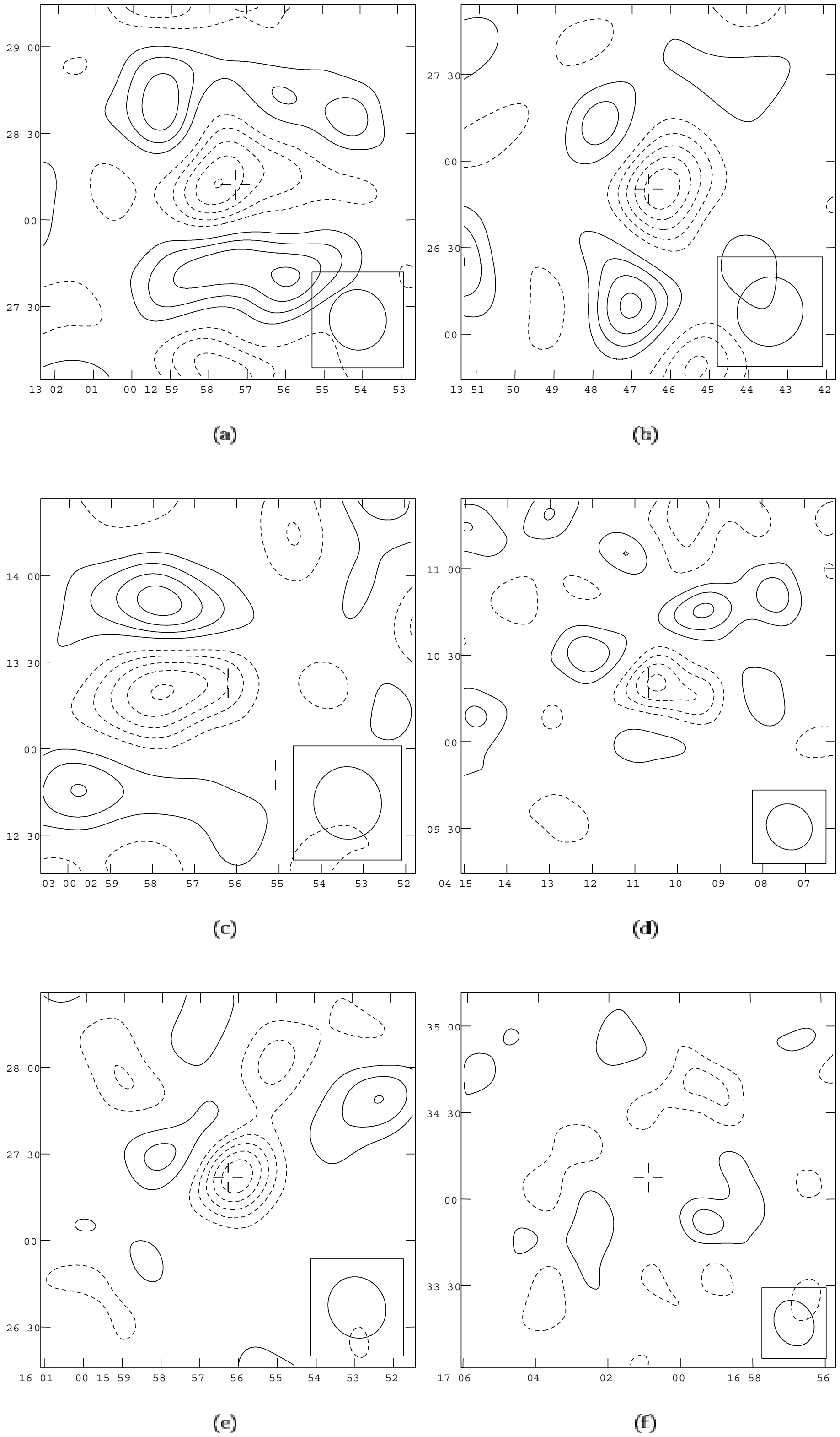

Figure 2. CLEANed VSA maps (a)–(f) of the clusters Coma, A1795, A399/A401 (where A399 is furthest south), A478, A2142 and A2244. The X-ray centre is marked in each case. The half-power CLEAN beam is shown in the bottom-right corner of each plot; contours are 1.5σ. Radio sources have been subtracted and the coordinates are B1950.

4.1.6 A2244: map (f)

A2244 does not appear in the map. Again, we suggest that the cluster may be coincident with a peak in the CMB.

4.2 Cluster model

In the SZ effect, incident CMB photons are Compton scattered by the hot gas in a cluster's potential well. At frequencies less than

217 GHz, a brightness temperature decrement in the microwave background is observed. This is proportional to the 'Comptonization parameter'

$$y = \frac{\sigma_{\mathrm{T}}}{m_{\mathrm{e}} c^2} \int n_{\mathrm{e}} k T \, \mathrm{d}l, \tag{1}$$

which is proportional to the line integral of pressure through the cluster. This can be calculated from modelled gas density distributions.

As we are working with specifically large angular scale SZ data, contamination from primordial CMB features is considerable, thus adding an extra 'noise' term. (In our parameter inference, this is dealt with appropriately as an additional source of Gaussian noise; see Section 4.4.) This restricts us to a highly constrained, simple model. We choose to follow Grego et al. (2001) in fitting a β-model (Cavaliere & Fusco-Femiano 1976, 1978) to the cluster visibilities. We too simplify the problem by assuming the clusters to be spherically symmetric and in hydrostatic equilibrium. [Note that strictly the assumptions of isothermality, β-profile, and hydrostatic equilibrium are incompatible. However, to good approximation, they are compatible over a wide range of r for β close to 2/3; see King (1962).] In the β-model, the gas density as a function of radius takes the form

$$\rho_{\mathrm{gas}}(r) = \frac{\rho_{\mathrm{gas}}(0)}{\left[1 + (r/r_{\mathrm{c}})^2\right]^{(3\beta)/2}}, \tag{2}$$

where r_{c} (core radius) and β are parameters of the fit. From the assumptions of hydrostatic equilibrium and gas isothermality at temperature T

$$\frac{kT}{\mu} \frac{\mathrm{d}\rho_{\mathrm{gas}}}{\mathrm{d}r} = -\rho_{\mathrm{gas}} \frac{G M_{\mathrm{r}}}{r^2}, \tag{3}$$

where M_{r} is the total mass internal to r, μ is the mass per particle, and k and G are the Boltzmann and gravitational constants, respectively. Equations (2) and (3) lead to the following expression for the total mass distribution:

$$M_{\mathrm{r}} = \frac{3\beta r^3}{\left(r_{\mathrm{c}}^2 + r^2\right)} \frac{kT}{\mu G}. \tag{4}$$

This can be adapted usefully to calculate cluster masses out to some overdensity (e.g. r_{200})

$$M_{200} = \frac{4\pi}{3} r_{200}^3 (200\rho_{\mathrm{crit}}) \tag{5}$$

$$= \frac{3\beta r_{200}^3}{\left(r_{\mathrm{c}}^2 + r_{200}^2\right)} \frac{kT}{\mu G}. \tag{6}$$

In this paper, we choose to calculate quantities out to r_{200} as this is a good approximation to the virial radius of a cluster. Previous studies have used r_{500} so we have also extended our calculations to produce results to this radius for comparison purposes.

From the gas density distribution (2), it is straightforward to compute the gas mass to this radius:

$$M_{\mathrm{gas}} = \int_0^{r_{200}} 4\pi r^2 \rho_{\mathrm{gas}} \, \mathrm{d}r \tag{7}$$

$$= 4\pi \rho_{\mathrm{gas}}(0) r_{\mathrm{c}}^3 \int_0^{r_{200}/r_{\mathrm{c}}} \frac{x^2 \, \mathrm{d}x}{(1 + x^2)^{(3\beta)/2}}. \tag{8}$$

The above integral is evaluated numerically. We choose to parametrize in terms of M_{gas}, and can solve for the gas density in order to compute the Comptonization parameter. The calculated values can then be compared to real VSA data.

The gas fraction is defined as

$$f_{\mathrm{gas}} = \frac{M_{\mathrm{gas}}}{M_{\mathrm{r}}}, \tag{9}$$

in which M_{gas} and M_{r} are evaluated to the same radius. f_{gas} evaluated by this method is proportional to h^{-1}. One way to see this is as follows. In equation (8), the h dependences of the limit r_{200}/r_{c} cancel, $\rho_{\mathrm{gas}}(0)$ is a local quantity and so not h-dependent, and only r_{c}^2 depends on h because the third factor of r_{c} is along the line of sight; thus $M_{\mathrm{gas}} \propto h^{-2}$. In equation (4), $M_{\mathrm{r}} \propto r^3/(r_{\mathrm{c}}^2 + r^2) \propto h^{-1}$. So, $f_{\mathrm{gas}} \propto h^{-1}$.

4.3 Interferometric data

Interferometers sample the *uv* plane, so it follows that the most straightforward approach is to fit to the visibility data directly. This is further motivated by the following points. The instrument noise is Gaussian in the *uv* plane, and independent between visibilities. In the map plane, the noise is highly correlated spatially. In addition, fitting to the visibilities naturally avoids the problem of synthesized beam deconvolution. The primordial CMB is well understood in the *uv* plane in terms of the measured power spectrum, so can be factored into the computation (see Section 4.4 for details). Finally, the inclusion of point sources is straightforward.

4.4 Contaminants

There are two relevant astrophysical contaminants to the SZ data: primordial fluctuations in the CMB and foreground radio sources. Emission from the Galaxy is taken to be negligible in this analysis.

Primordial CMB fluctuations, recognized as a source of Gaussian noise with known angular power spectrum, are included in a non-diagonal covariance matrix when calculating the misfit between predicted and observed data (Reese et al. 2002; Marshall, Hobson & Slosar 2003). We observed bright primordial features in all of our cluster maps, and indeed they are evident in Fig. 2. As the negative primordial features are of similar strengths and on similar angular scales to the cluster decrements, it is necessary to apply fairly tight positional priors (see Section 4.5). As regards f_{gas} estimates, we argue that the position is acceptable as the effect of the CMB tends to produce a cancelling effect on M_{gas} and M_{r} (see Section 4.6).

The point sources present in each field are also included in the model of the sky. The source-subtractor data allow the determination of the fluxes and positions of these objects; we translate these measurements into appropriate priors (see Section 4.5) on the source parameters. These 'nuisance parameters' are then marginalized out.

4.5 Parameter inference

4.5.1 Basic considerations

In inferring cluster parameters, the traditional route followed in the literature is the maximum likelihood method. This method was used in, for example, the SZ and gas fraction work of Grego et al. (2001). Computational restrictions at the time prevented the use of the fully Bayesian analysis we perform in this paper. The likelihood of a data set $L(\mathrm{data}|\boldsymbol{\theta})$ is the product of the probability distributions of the constituent data points, where $\boldsymbol{\theta}$ is used to characterize a set of parameters such as β and core radius. This likelihood may be maximized to find the best-fitting value for each parameter of the set $\boldsymbol{\theta}$.

(i) This approach assumes that the parameters $\boldsymbol{\theta}$ of a model have a true set of values, and that obtaining data from an appropriate experiment will measure this set of values.

(ii) This approach can be formulated in terms of a single misfit statistic when describing the difference between the predictions of a model and a measurement; maximizing a Gaussian likelihood for data with uncorrelated errors is equivalent to minimizing the mean-squared residual, or χ^2 statistic.

(iii) This approach usually assumes Gaussian noise, although indeed this can be modified to incorporate the correct distribution (e.g. Poisson) for a particular case.

The maximum likelihood method focuses on the estimation of true parameters from data, while neglecting the full distributions for those parameters. When the signal-to-noise ratio is low, these distributions are broad and very unlikely to be Gaussian. We summarize the difficulties in this situation as follows.

Maximum likelihood does not describe the joint process of observation and inference. We have a set of noisy visibilities (the data) which we attempt to explain by a model or hypothesis, H. The hypothesis includes the notions, for example, that the SZ signal comes from a gas distribution (which we assume here to have a β-profile) and that sources and CMB primordials are present, and also the assumption that we understand the experiment in question (i.e. the interferometer works). The data model includes the parameter set $\boldsymbol{\theta}$ as defined above. We wish to estimate $\boldsymbol{\theta}$ from our data; that is, we wish to examine the probability distribution $P(\boldsymbol{\theta}|\text{data, H})$. Note that the notation $P(\text{A}|\text{B})$ refers to the probability of A given B. Rather than achieving this, the maximum likelihood method assesses the data while taking it as given that $\boldsymbol{\theta}$ has some true value, as outlined in point (i) above. In other words, it evaluates just the peak of the probability distribution $P(\text{data}|\boldsymbol{\theta}, \text{H})$. Application of Bayes theorem allows us to relate the two distributions $P(\boldsymbol{\theta}|\text{data, H})$ (the posterior) and $P(\text{data}|\boldsymbol{\theta}, \text{H})$ by

$$P(\boldsymbol{\theta}|\text{data, H}) = \frac{P(\text{data}|\boldsymbol{\theta}, \text{H})P(\boldsymbol{\theta}|\text{H})}{P(\text{data}|\text{H})}. \qquad (10)$$

The additional factors in equation (10) are the 'prior' probability distribution, $P(\boldsymbol{\theta}|\text{H})$, and the 'evidence', $P(\text{data}|\text{H})$, to which we will return shortly.

In addition, point (ii) is not generally correct. Even if $P(\text{data}|\boldsymbol{\theta}, \text{H})$ is Gaussian, it is multiplied by the prior $P(\boldsymbol{\theta}|\text{H})$, which may, for example, be asymmetric. Once one starts to produce resultant probability density functions by multiplication the distributions are certainly going to be complicated. The probabilities outlined above are 'functions'. The standard maximum likelihood approach characterizes such probability distributions by a single value with an error bar. The characterization of probability distributions with approximate Gaussians is therefore misleading and may underestimate the final uncertainty in a quantity such as f_{gas}. It is clearly preferable to retain all the information contained in the entire function, rather than working with single-value parameters. As mentioned above, point (iii) can be dealt with appropriately.

Propagating the likelihood function via Bayes theorem thus overcomes points (i) and (ii) above. It also delivers additional advantages, summarized as follows.

(i) Conditioning on a particular value of a parameter implies a delta-function prior, a state of knowledge that never occurs. It is now possible to deal with continuous probability distribution functions in many dimensions (e.g. positions, core radii, M_r, etc.) rather than having to work just with peaks and widths of artificially low-dimensional probability distributions. A desire to concentrate on a subset of interesting parameters leads directly to the concept of marginalization (see, for example, Sivia 1996).

(ii) The method leads directly to the evaluation of the evidence, an extremely useful quantity that enables one to assess the relative suitability of a set of hypotheses (see, for example, Hobson, Bridle & Lahav 2002).

The evidence in equation (10) is $P(\text{data}|\text{H})$ and is an integral over all parameters in the N-dimensional parameter vector $\boldsymbol{\theta}$:

$$P(\text{data}|\text{H}) = \int P(\text{data}|\boldsymbol{\theta}, \text{H})P(\boldsymbol{\theta}|\text{H})\text{d}^N\boldsymbol{\theta}. \qquad (11)$$

This can be applied usefully to help distinguish between different hypotheses, say H_1 and H_2; Bayes theorem (equation 10) can be applied in order to evaluate and compare $P(\text{H}_1|\text{data})$ and $P(\text{H}_2|\text{data})$. In doing this, $P(\text{data})$ cancels out and we obtain

$$\frac{P(\text{H}_1|\text{data})}{P(\text{H}_2|\text{data})} = \frac{P(\text{data}|\text{H}_1)}{P(\text{data}|\text{H}_2)}\frac{P(\text{H}_1)}{P(\text{H}_2)}. \qquad (12)$$

Thus, hypotheses may be compared. For example, we can evaluate the hypothesis that an SZ cluster is in a particular, small patch of sky. We can compare this with the evidence given an alternative hypothesis, this time deeming that the cluster be found in a larger area of sky. The hypothesis probability ratio given in equation (12) provides the means by which the suitability of these two priors can be assessed. Such additional information may be obtained from elsewhere; in this particular example, X-ray data may be used to good effect.

We note that both maximum likelihood and Bayesian methods can cope with correlated data (see, for example, Reese et al. 2002; Marshall et al. 2003, as before) but simple χ^2 minimization cannot.

4.5.2 Characterizing the posterior probability density function

Having summarized the advantages of the Bayesian route, we now turn to the problem of calculating the posterior distribution $P(\boldsymbol{\theta}|\text{data, H})$. One method is to evaluate it as a product of the probabilities for every visibility, for all possible values of each of the N parameters in $\boldsymbol{\theta}$. This is the 'brute force' approach, involving the calculation of the likelihood over a huge hypercube. This technique is now plausible for application to the CMB primordial power spectrum, given that the CMB itself has a Gaussian brightness probability distribution at every point on the sky (and is indeed the same everywhere). However, it is not a realistic approach for an SZ β-model with position, mass and size uncertainties in the presence of the CMB and a number of radio sources. So we have chosen to represent the posterior in an approximate way by drawing samples from it, the MCMC method; see, for example, Gilks, Richardson & Spiegelhalter (1996) and Ó Ruanaidh & Fitzgerald (1996) for general introductions, and Marshall et al. (2003) and Bonamente et al. (2004) for galaxy cluster specifics.

This process results in a set of sample parameter vectors whose number density is proportional to the posterior probability, such that all local maxima are explored in proportion to their relevance. In order to ensure that the correct regions of parameter space are being probed, sufficient samples must be taken and calculations made. This is problematic in that it must be both accurate and efficient; to this end, we use the commercially available sampler BAYESYS

(Skilling 2002), a powerful code designed to be flexible enough to cope with a wide range of problems. BAYESYS makes use of a range of proposal distribution 'engines' that govern where next to sample, and in particular employs those that it finds dynamically to be most efficient for a particular posterior probability density function. In addition, it should be possible to assess whether or not enough evaluations have been performed over an acceptable range of $\boldsymbol{\theta}$, that is when the process has 'burnt in'. A review of such tests is given in Cowles & Carlin (1996). We follow Marshall et al. (2003) and argue that several short, independent burn-ins are a good idea to check that they agree. The diagnostic we use is the evidence itself, which we calculate by 'thermodynamic integration' (see, for example, Ó Ruanaidh & Fitzgerald 1996). The method works as follows. The evidence (as given in equation 11) is

$$P(\mathrm{data}|\mathrm{H}) = \int P(\mathrm{data}|\boldsymbol{\theta}, \mathrm{H}) P(\boldsymbol{\theta}|\mathrm{H}) \mathrm{d}^N\boldsymbol{\theta} \equiv E(1). \tag{13}$$

We now write

$$E(\lambda) = \int P^{\lambda}(\mathrm{data}|\boldsymbol{\theta}, \mathrm{H}) P(\boldsymbol{\theta}|\mathrm{H}) \mathrm{d}^N\boldsymbol{\theta}. \tag{14}$$

BAYESYS allows the running in parallel of several Markov chains (typically 10 in our case). The key to the method is as follows. The sampling starts with $\lambda = 0$. This means that the new data are initially ignored, with samples just being drawn from the prior. At this stage, remote regions of parameter space (that are at least allowed by the prior) are sampled. λ is then gradually raised to one, at a rate balancing the needs for computational speed and accuracy in the log evidence calculation. The latter can be shown to reduce to the numerical integral of the ensemble-averaged log-likelihood with respect to λ (Ó Ruanaidh & Fitzgerald 1996).

4.5.3 *Practicalities*

It is always of utmost importance to ensure that one does not over-interpret the data available. This is crucial here, as we have not only fairly noisy data (due to the faint nature of the effect being studied), but also considerable contamination from point sources and primordial CMB fluctuations. As is evident in the VSA data (Fig. 2), and previously mentioned in Section 4.4, CMB features may be comparable in strength to the SZ decrement itself. It would be quite possible to fit, accidentally, to a negative CMB feature, which would be very misleading. Our method avoids this danger by including all contaminants in the model, and fitting all parameters simultaneously. We have chosen to fit a simple but well-motivated model to our data, but even so we must fit six parameters plus source fluxes and positions. This makes the task computationally expensive (vastly more so than using maximum likelihood). In order to extract parameters for a single cluster, around 100 h of computer time is required (2 GHz processor). We do not expect to place tight constraints on, for example, β or r_c and we anticipate broad probability distributions for all parameters. However, when we marginalize properly over all parameters we find some interesting precisions on f_gas.

In order to compare a sample model with the VSA data, we project the model gas pressure and map the Comptonization on to a grid. A fast Fourier transform is then performed, and interpolated on to the uv coordinates. These predicted visibilities are then compared to the observed cluster visibilities. Working directly with the visibilities has the advantages described in Section 4.3. We deal with point sources and the CMB in the following natural way. The Fourier transform of a delta function is a constant amplitude sine wave. This can be used to increment all the predicted visibilities by a factor specific to each source's sample parameters. The uncertainty on each measured visibility is Gaussian and has contributions from both the thermal noise in the receivers (which is uncorrelated) and the primordial CMB fluctuations (which are correlated between adjacent points in the u–v plane). The resultant noise covariance matrix C is non-diagonal but calculable given a primordial power spectrum, assumed to be well known. The likelihood of the visibility data is therefore

Table 3. Priors for the cluster analysis. Positions and gas temperatures for individual clusters are quoted in Table 1.

Parameter	Prior
Position	Gaussian, 1 arcmin
r_c	Uniform, 1–1000 kpc
β	Uniform, 0.3–1.5
T_e	Gaussian, ASCA value ±15 per cent
M_gas	Uniform, $(0.01 - 3.00) \times 10^{14}$

$$P(\boldsymbol{d}|\boldsymbol{\theta}, \mathrm{H}) = \frac{1}{(2\pi)^{N_\mathrm{vis}}|\mathsf{C}|^{1/2}} \exp\left[-(\boldsymbol{d} - \boldsymbol{d}_\mathrm{p})^T \mathsf{C}^{-1} (\boldsymbol{d} - \boldsymbol{d}_\mathrm{p})\right], \tag{15}$$

where $\boldsymbol{d}$ and $\boldsymbol{d}_\mathrm{p}$ represent the observed and predicted visibility vectors respectively, and N_vis is the number of visibilities.

The priors used to characterize the various model parameters are summarized in Table 3. As mentioned in Section 4.4, tight priors were placed on both the cluster position, and point source positions and fluxes. For the cluster centroid, the X-ray centre (Böhringer et al. 2000) was included as a Gaussian prior of width 1 arcmin. We chose to place a weak prior on the core radius such that it be determined by the data to hand. The prior on the β parameter encompasses the extremes of the range of values found in clusters to date. The temperature prior allows a generous error on the fit. Note that f_gas depends on T^2 (see Grego et al. 2001). The prior on the gas mass more than encompasses the accessible range. The point source fluxes included in the model were also assigned Gaussian priors, based on the source-subtractor measurements and their uncertainty. The prior on each source flux was broadened to account for variability of a factor of 1.33 times the measured flux; this step was only taken when the epoch of the source measurement was significantly different from that of the cluster observation. For the sources selected using predictions from lower frequencies, positional accuracies were taken from the GB6 catalogue. The sources detected in the RT surveys were assumed to have positional uncertainty of ±40 arcsec in both RA and Dec.; this is wide enough to cover even the weakest sources.

4.6 Effect of primordials on f_gas estimates

In the context of large angular scale SZ observations, the CMB is additional noise which will provide a source of error in the determination of f_gas. This extra noise was dealt with correctly when calculating cluster parameters (see Section 4.4). However, here we present a simple argument describing why, in situations where the SZ data are used to infer both the gas mass and the total mass (as discussed in Section 4.2), the contamination is not as catastrophic as one may anticipate. With the present data quality, fitting a β-model is doing little more than fitting an offset plus a slope. If there is more negative signal due to a negative CMB feature coinciding with the cluster position, then the M_gas estimate will be higher. (Note that this is a simplistic argument because of course the contribution to the

Table 4. Gas fraction estimations for A478 with the inclusion of a test contaminant source of flux $S_{\rm add}$ at the cluster centre.

$S_{\rm add}$ (mJy)	$f_{\rm gas}$
-100	$0.056^{+0.088}_{-0.041}$
-50	$0.10^{+0.12}_{-0.06}$
-25	$0.12^{+0.14}_{-0.07}$
0	$0.12^{+0.11}_{-0.06}$
25	$0.13^{+0.14}_{-0.07}$
50	$0.11^{+0.13}_{-0.06}$
100	$0.10^{+0.09}_{-0.05}$

Comptonization parameter depends on the mass distribution which is linked to the total mass.) Now, in estimating $M_{\rm r}$, the effect of the above will be to increase the central concentration, increasing β or decreasing $r_{\rm c}$. Examination of equation (8) shows that this effect will increase an estimation of $M_{\rm r}$. So, in this type of scenario, as both $M_{\rm gas}$ and $M_{\rm r}$ will be higher, the effects of the CMB tend to cancel out when calculating $f_{\rm gas}$ for the cluster in question. A similar effect is observed for a bright primordial feature – the SZ signal will tend to decrease, and β will also decrease as the cluster will appear to be less centrally condensed. Thus, if the primordial CMB contamination happens to be correlated over the measured u range, then the effects on $M_{\rm gas}$ and $M_{\rm r}$ tend to cancel, leaving $f_{\rm gas}$ little affected.

In general, depending on the actual sizes, shapes and positions of the primordial features behind the SZ decrement, $f_{\rm gas}$ may be pushed higher or lower, or remain relatively unaffected as outlined above. Of course, if there is a universal value of $f_{\rm gas}$, then combining the results from a reasonable number of clusters will both help reduce any remaining effects and also help to evaluate the effect's magnitude. One may intuitively regard the cases presented above to be the 'worst-case scenario', when in fact they appear not to cause too great a difficulty.

We have performed a simple simulation in order to examine this cancelling effect semiquantitatively. Using our A478 data, we placed a test source of flux $S_{\rm add}$ at the pointing centre and recalculated $f_{\rm gas}$. Results for test sources in the range $-100 > S_{\rm add} > 100$ mJy are presented in Table 4. Although this is by no means a rigorous test of the argument postulated, we note that the values of $f_{\rm gas}$ for all $S_{\rm add}$ are consistent within errors. This indicates that in this context (i.e. for our uv range and chosen cluster sample), the effect of the CMB tends to cancel out in this context. Note that typical SZ fluxes are ≈150 mJy, whereas CMB plus receiver noise will typically produce features of ≈100 mJy, and occasionally >150 mJy. From these simple calculations, we argue that estimations of $f_{\rm gas}$ should be relatively unaffected by the presence of primordial CMB in all but the worst cases.

4.7 Other effects on $f_{\rm gas}$

In this work, the random errors present are larger than any systematics, but here we present a brief discussion of some possible additional sources of error. Our assumptions of isothermality and sphericity may affect our inferred values for $f_{\rm gas}$. If a cluster were not isothermal, we may, for instance, overestimate the temperature in the outer regions due to a temperature gradient, and may overestimate both the gas and total mass with a possible small net underestimate of the gas fraction. Regarding asphericity, which we do not expect to have a large effect because we are not using X-ray surface brightness, we point out that our sample is orientation unbiased, because our flux limit is well above the flux limit of the X-ray survey from which the clusters were chosen. Grego et al. (2001) made mock observations of a simulated cluster population, finding no bias as a result of using a spherical isothermal β-model, suggesting that these two sources of systematic error indeed may not be significant in this work. Additionally, Arnaud, Pratt & Pointecouteau (2004) find that the temperature variation for clusters observed with *XMM–Newton* is less than 10 per cent out to half the virial radius. Similarly, Zhang et al. (2004) find errors on mass estimates from *XMM–Newton* data to be less than 25 per cent as a result of temperature gradients. Generally, X-ray derived pressure maps seem to show a factor of 2 less variation (for example, azimuthally around the cluster centre) than either density or temperature maps. Still, gas clumping could be a problem. Clumps, if unresolved, will lead to enhanced signal in an X-ray map and thus bias the cluster temperature. This will artificially increase the inferred total mass. However, the SZ data themselves are less sensitive to clumping as the SZ signal is proportional to $n_{\rm e}$ rather than $n_{\rm e}^2$. Ultimately, the comparison of high signal-to-noise ratio SZ data with X-ray measurements will constrain the level of clumping in clusters.

4.8 Cluster parameters

We discuss the constraints placed on the core radius and β-parameter by the VSA data, and we also present results for the gas mass, total mass and gas fractions calculated out to both r_{200} and r_{500}. For comparison, a summary of cluster parameters derived from X-ray data is presented in Table 5.

Table 5. Cluster parameters derived from X-ray data. References are [1] Mason & Myers (2000), [2] Mohr et al. (1999) and [3] Sanderson & Ponman (2003).

	$r_{\rm c}$ (arcmin)		β			n_0	
						$(10^{-3}\,h_{100}^{1/2}\,{\rm cm}^{-3})$	$(10^{-3}\,h_{50}^{1/2}\,{\rm cm}^{-3})$
	[1]	[3]	[1]	[2]	[3]	[1]	[2]
Coma	9.32 ± 0.10	–	0.670	$0.705^{+0.046}_{-0.046}$	–	$4.51^{+0.04}_{-0.04}$	$3.12^{+0.04}_{-0.04}$
A1795	2.17 ± 0.28	$4.01^{+0.20}_{-0.21}$	0.698	$0.790^{+0.031}_{-0.032}$	0.83 ± 0.02	$11.29^{+0.61}_{-1.77}$	$29.9^{+4.6}_{-1.5}$
A399	4.33 ± 0.45	$1.89^{+0.36}_{-0.36}$	0.742	–	0.53 ± 0.05	$3.24^{+0.14}_{-0.19}$	–
A401	2.26 ± 0.41	$2.37^{+0.09}_{-0.09}$	0.636	$0.606^{+0.015}_{-0.016}$	0.63 ± 0.01	$8.01^{+0.56}_{-1.02}$	$5.87^{+0.43}_{-0.27}$
A478	1.00 ± 0.15	$2.34^{+0.23}_{-0.23}$	0.638	$0.713^{+0.030}_{-0.033}$	0.75 ± 0.01	$28.9^{+15.2}_{-3.9}$	$38.1^{+3.3}_{-1.5}$
A2142	1.60 ± 0.12	$3.14^{+0.22}_{-0.22}$	0.635	$0.787^{+0.082}_{-0.093}$	0.74 ± 0.01	$15.03^{+0.92}_{-1.07}$	$15.8^{+1.7}_{-2.4}$
A2244	0.82 ± 0.14	–	0.580	$0.594^{+0.061}_{-0.045}$	-	$17.73^{+1.95}_{-2.65}$	$13.2^{+1.9}_{-2.9}$

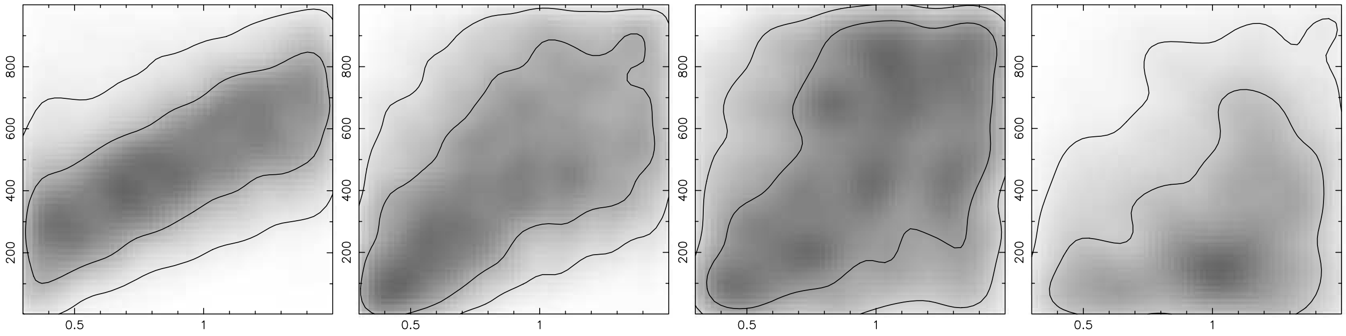

(a)Coma (b)A1795 (c)A399 (d)A401

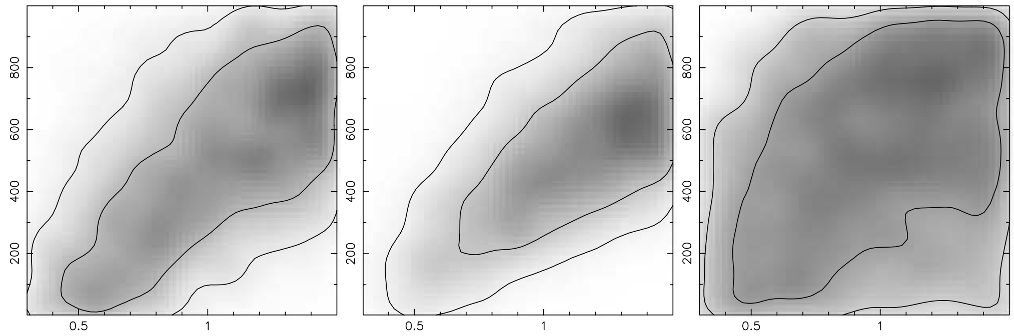

(e)A478 (f)A2142 (g)A2244

Figure 3. Plots illustrating the constraints placed on β-parameter and core radius by the cluster data. In each plot, the *x*-axis is β and the *y*-axis is core radius (kpc). 68 and 90 per cent contours are shown.

Table 6. Gas masses, total masses and gas fractions for the VSA cluster sample evaluated to both r_{200} and r_{500}.

Cluster	$M_{\mathrm{gas}}(r_{200})\,h^2$ 10^{13} M$_{\odot}$	$M_{\mathrm{gas}}(r_{500})\,h^2$ 10^{13} M$_{\odot}$	$M_{\mathrm{r200}}h$ 10^{14} M$_{\odot}$	$M_{\mathrm{r500}}h$ 10^{14} M$_{\odot}$	$f_{\mathrm{gas}}(r_{200})h$	$f_{\mathrm{gas}}(r_{500})h$
Coma	$15.4^{+9.0}_{-8.0}$	$6.6^{+3.5}_{-3.0}$	$10.9^{+10.0}_{-6.0}$	$5.2^{+5.5}_{-3.1}$	$0.15^{+0.28}_{-0.10}$	$0.15^{+0.17}_{-0.09}$
A1795	$8.5^{+3.9}_{-3.4}$	$3.5^{+1.6}_{-1.7}$	$7.9^{+6.5}_{-4.1}$	$3.4^{+3.7}_{-2.0}$	$0.12^{+0.15}_{-0.070}$	$0.11^{+0.090}_{-0.060}$
A399	$1.9^{+2.4}_{-1.3}$	$0.7^{+1.1}_{-0.6}$	$7.6^{+5.3}_{-3.9}$	$3.1^{+3.6}_{-2.0}$	$0.030^{+0.054}_{-0.022}$	$0.028^{+0.040}_{-0.020}$
A401	$5.0^{+3.0}_{-2.3}$	$3.0^{+1.4}_{-1.4}$	$10.7^{+6.0}_{-5.0}$	$5.8^{+4.2}_{-3.4}$	$0.048^{+0.074}_{-0.028}$	$0.055^{+0.055}_{-0.029}$
A478	$11.2^{+4.0}_{-4.0}$	$5.7^{+2.1}_{-2.2}$	$10.8^{+6.0}_{-5.0}$	$4.8^{+3.7}_{-2.5}$	$0.12^{+0.11}_{-0.06}$	$0.13^{+0.08}_{-0.05}$
A2142	$11.2^{+4.0}_{-3.0}$	$6.1^{+1.7}_{-1.8}$	$15.3^{+8.0}_{-6.0}$	$7.3^{+4.6}_{-3.4}$	$0.074^{+0.068}_{-0.034}$	$0.086^{+0.056}_{-0.035}$
A2244	$1.3^{+1.6}_{-0.8}$	$4.4^{+8.4}_{-3.7}$	$7.5^{+5.8}_{-3.8}$	$3.0^{+3.8}_{-2.1}$	$0.020^{+0.039}_{-0.015}$	$0.020^{+0.031}_{-0.014}$

We find, as anticipated, that the cluster parameters β and r_{c} are poorly constrained by the SZ data, as shown in Fig. 3. For Coma, A1795, A478 and A2142, there is considerable degeneracy between the two parameters. It is only possible to place limits on the two parameters together – little can be said about them as separate entities. This is largely due to the limited range of angular scales presented in these data, and indeed in any SZ data to date. Ideally, one would combine the VSA data with observations on smaller angular scales. This is impossible in this case, as instruments such as the RT would completely resolve out the signal from the clusters in our sample. The Arcminute MicroKelvin Imager (AMI; see, for example, Kneissl et al. 2001) will work over a larger range of angular scales and should start to break this degeneracy. A401, A399 and A2244 are not detected in the cluster maps, so it is perhaps unsurprising that little constraint can be placed upon the shape parameters by these data.

We present the median of the probability distribution for the gas mass, total mass and gas fraction for each cluster, evaluated to both r_{200} and r_{500}, in Table 6. The errors quoted are the values of the 16.5th and the 83.5th percentiles. We note that A1795, A478 and A2142 all favour a gas mass of around 10^{14} M$_{\odot}$. The Coma data allow very high gas masses. This may be interpreted as the cluster position coinciding with a negative feature in the CMB, thus making the SZ decrement appear deeper. The converse may be true for the other three clusters, in that their SZ signals may be partially 'obscured' by hotspots in the CMB. If this were true, it would have

Table 7. Gas fractions estimated within R_0 from SZ data ([1] Myers et al. 1997), and within r_{500} from X-ray data ([2] Mason & Myers 2000; [3] Mohr et al. 1999; [4] Ettori & Fabian 1999).

	$f_{\rm gas}h$ [1]	R_0h(Mpc) [1]	$f_{\rm gas}\,h^{3/2}$ [2]	$f_{\rm gas}\,h_{50}^{3/2}$ [3]	$f_{\rm gas}\,h_{50}^{3/2}$ [4]
Coma	0.063 ± 0.017	1.50	0.0603 ± 0.0028	0.177 ± 0.019	–
A1795	–	–	0.0477 ± 0.0036	0.190 ± 0.008	0.184 ± 0.011
A399	–	–	0.0655 ± 0.0032	–	–
A401	–	–	$0.0794^{+0.0044}_{-0.0062}$	0.247 ± 0.012	0.230 ± 0.013
A478	0.166 ± 0.014	0.976	$0.0760^{+0.0076}_{-0.0045}$	$0.214^{+0.012}_{-0.011}$	0.172 ± 0.023
A2142	0.060 ± 0.011	0.76	$0.0890^{+0.0064}_{-0.0091}$	$0.227^{+0.024}_{-0.017}$	0.255 ± 0.033
A2244	–	–	$0.0739^{+0.0170}_{-0.0349}$	$0.196^{+0.061}_{-0.060}$	0.204 ± 0.104

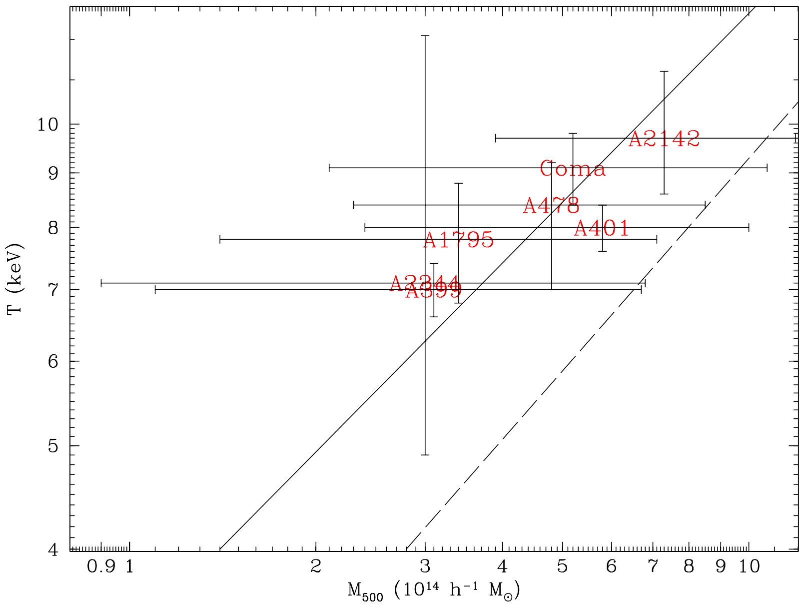

Figure 4. The mass–temperature scaling relation derived from fitting gas pressure profiles to the VSA SZ data. The temperature shows the X-ray temperatures given in Table 1 and also enters M_{500} linearly. The dashed line uses the normalization from hydrodynamical adiabatic simulations (Evrard et al. 1996), and the solid line represents the best-fitting M–T relation of Finoguenov et al. (2001).

the effect of reducing the preferred values of the gas mass, and indeed these objects do allow low values of this parameter. [Note that although here we choose to follow Myers et al. (1997) in using X-ray temperatures from Markevitch et al. (1998), we recognize that more recent data are available. Repeating the analysis using *XMM–Newton* temperatures (Sun et al. 2003; Pointecouteau et al. 2004) we find that the resulting $f_{\rm gas}$ values are fully consistent with those presented in Fig. 5 and Table 7. Any variations are below the random errors present in the VSA data.]

It is interesting to examine the constraints placed on the relationship between total mass $M_{\rm r}$ and gas temperature by the VSA SZ data. In Fig. 4 we plot the X-ray determined temperature and the total mass $M_{\rm r}$ derived using equation (6). We expect, of course, some scatter on the values of $M_{\rm r}$ for each cluster due to the CMB contamination of the SZ data. After examination of equation (6), we argue that the normalization of our M–T relation is, in fact, mainly determined by the profile fitting parameters β and $r_{\rm c}$ derived from the VSA data, and depends only weakly on $T_{\rm X}$($T_{\rm X}^{-1/2}$ for the self-similar 3/2 slope of the M–T relation). This means in Fig. 4 that the effect of any uncertainty in T (and consequently in M_{500}) for a given set of β, $r_{\rm c}$ from the VSA will move the data points within their large error boxes almost parallel to the slope of the M–T relation. For comparison, we plot the normalization of the M–T relations from hydrodynamical adiabatic simulations (Evrard, Metzler & Navarro 1996) and X-ray cluster data (Finoguenov, Reiprich & Böhringer 2001). We calculate our normalization constant for $M \propto T^{3/2}$ to be $2.33^{+0.85}_{-0.78} \times 10^{13}$. This is in good agreement with the recent M–T determinations derived from X-ray data (Allen, Schmidt & Fabian 2001; Pratt & Arnaud 2002). In a forthcoming paper we intend to investigate the possibility of determining the M–T relation from SZ without the use of an X-ray temperature. Such an M–T relation, based on a measurement of the global gas pressure distribution via the SZ effect, will be interesting to contrast with X-ray measurements. This type of work will be very useful for the interpretation of upcoming SZ cluster surveys.

The $f_{\rm gas}$ probability distributions are highly non-Gaussian, and are plotted on the same axes in Fig. 5. The errors quoted are the values of the 16.5th and the 83.5th percentiles. In order to compare values for individual clusters, we summarize results from other experiments in Table 7.

We have combined the posterior probability density functions for each cluster gas fraction as follows (see Marshall, in preparation,

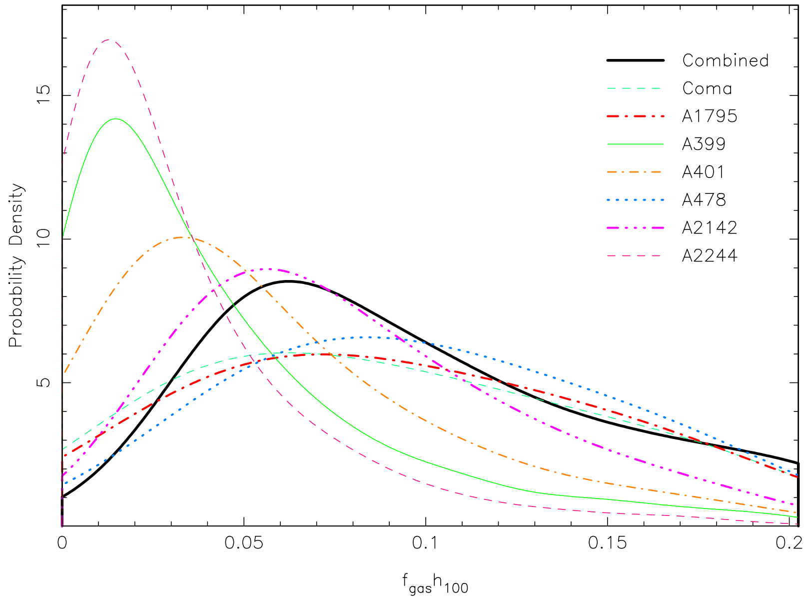

Figure 5. Plot of the probability distributions for $f_{\rm gas}$ for each cluster, and that derived from combining the full sample.

for more details). Simulating the effect of simultaneously fitting all our SZ data with the same global gas fraction $f_{\rm gas}$ requires dividing out the prior on the individual cluster gas fraction (which can be derived from a set of MCMC samples with no data; see Slosar et al. 2003) and then multiplying the resulting effective likelihoods together. Modulating this product by the prior on $f_{\rm gas}$, which we take to be uniform over the range [0–0.2], gives us the posterior probability density function $P(f_{\rm gas}|{\rm data})$. Moreover, keeping track of the normalizations allows us to compute a relative probability for the act of combination itself, that is, the ratio $P({\rm data}|{\rm H}^{\rm global})/P({\rm data}|\,{\rm H}^{\rm i})$. Here, ${\rm H}^{\rm i}$ is the hypothesis 'all clusters have independent gas fractions $f^{\rm i}_{\rm gas}$', whilst ${\rm H}^{\rm global}$ is the alternative hypothesis that 'all clusters have the same gas fraction $f_{\rm gas}$'.

We first assume that all our clusters have one true global gas fraction value, $f_{\rm gas}$. We combine the individual probability density functions for all of our clusters, including those with what would classically be called non-detections. We find $f_{\rm gas}\,h_{100} = 0.023^{+0.016}_{-0.012}$, with an evidence ratio in favour of this all-encompassing combination of

$$\frac{P({\rm data}|{\rm H}^{\rm global})}{P({\rm data}|{\rm H}^{\rm i})} = 4.4. \tag{16}$$

We can also divide the data into two sets, those from detected clusters and those from non-detections, and again investigate the suitability of their combination. Let hypothesis ${\rm H}^{\rm global}_{\rm det}$ consist of the assertions that there is a global gas fraction $f_{\rm gas}$ exhibited by the detected clusters, and that there is another gas fraction-like parameter X for the non-detections. We find the following evidence ratios:

$$\frac{P\left[{\rm data(detections)}|{\rm H}^{\rm global}_{\rm det}\right]}{P[{\rm data(detections)}|{\rm H}^{\rm i}]} = 0.92, \tag{17}$$

$$\frac{P\left[{\rm data(non\text{-}detections)}|{\rm H}^{\rm global}_{\rm det}\right]}{P[{\rm data(non\text{-}detections)}|{\rm H}^{\rm i}]} = 7.41. \tag{18}$$

The former suggests that the data are not good enough to distinguish between the global gas fraction hypothesis and that of all four detected clusters taking independent values of $f^{\rm i}_{\rm gas}$. However, the latter points strongly towards the combination of the non-detection gas fractions. The overall evidence ratio from this 'split sample' analysis is therefore

$$\begin{aligned}\frac{P\left[{\rm data(all)}|{\rm H}^{\rm global}_{\rm det}\right]}{P[{\rm data(all)}|{\rm H}^{\rm i}]} &= \frac{P\left[{\rm data(detections)}|{\rm H}^{\rm global}_{\rm det}\right]}{P[{\rm data(detections)}|{\rm H}^{\rm i}]}\\ &\quad\times \frac{P\left[{\rm data(non\text{-}detections)}|{\rm H}^{\rm global}_{\rm det}\right]}{P[{\rm data(non\text{-}detections)}|{\rm H}^{\rm i}]}\\ &= 6.82.\end{aligned} \tag{19}$$

This is higher than the result in equation (16), indicating that the split sample analysis is more appropriate. The interpretation is that the detected clusters are telling us about a global cluster gas fraction $f_{\rm gas}$, while the non-detections are telling us far more about the primordial fluctuations (inappropriately parametrized by X). Our 'headline' result is therefore that from combining the gas fractions of the four detected clusters as above: $f_{\rm gas}\,h_{100} = 0.08^{+0.06}_{-0.04}$.

In order to address the true value of a global $f_{\rm gas}$ we need better data, which the likes of AMI (see, for example, Kneissl et al. 2001), Array for Microwave Background Anisotropy (AMiBA; see, for example, Lo 2002) and the Sunyaev–Zel'dovich Array (SZA; see, for example, Mohr et al. 2002) should provide. We have however developed and demonstrated a useful method for estimating the effect of, and for controlling, systematics. We could do even better in estimating a universal $f_{\rm gas}$ if we were able to use prior information (from X-rays and lensing) on the likely detectability in SZ of each cluster. This would require us to be able to separate the 'position' and 'existence' implicit in the priors we use; we are planning to attempt this.

We can also place formal constraints on $\Omega_{\rm m}h$ by assuming that our estimation for $f_{\rm gas}h$ is indeed the global value:

$$f_{\rm gas}h = \frac{\Omega_{\rm b}h^2}{\Omega_{\rm m}h}. \tag{20}$$

Rebolo et al. (2004) infer $\Omega_{\rm b}\,h^2$ and h_{100} from VSA and *WMAP* primordial CMB data, using a flat ΛCDM model. We take these values and find $\Omega_{\rm m}\,h = 0.33^{+0.33}_{-0.15}$.

Another implication concerns the clumping of the cluster gas. The broad agreement here between $f_{\rm gas}$ values from X-ray and from SZ, and as discussed, for example, in Grego et al. (2001), rules out significant clumping.

5 CONCLUSION

We have investigated with the VSA Extended Array at ≈34 GHz the SZ effects towards seven nearby clusters that form a complete, X-ray flux-limited sample.

(i) Four of the clusters (Coma, A1795, A478, A2142) show SZ effects in the map plane on scales of ≈20 arcmin of typically 6σ.

(ii) There is significant detection of CMB primordial structure at this resolution, which is the likely cause of the three non-detections (A399, A401, A2244).

We have analysed the data in the *uv* plane, with X-ray priors on positions and gas temperatures and radio priors on the sources, using the MCMC method to estimate key cluster parameters in the context of a β-model for the gas distribution. In this context, the CMB primordial fluctuations are an additional source of Gaussian noise, and are included in the model as a non-diagonal covariance matrix derived from the known angular power spectrum. We use the SZ data (plus the priors) to give both the gas mass and, under the assumption of hydrostatic equilibrium, the total mass. Although the data have high random errors, the use of Bayesian methods, probability density functions and marginalization prevents bias in the results.

(iii) The degeneracy is evident between β and core radius as expected for such observations sensitive to SZ over a narrow ℓ-range. There are significant measurements of gas fractions in the detected clusters.

(iv) We present a normalization of the M–T relation derived from our data, which we find to be in good agreement with recent X-ray cluster measurements.

(v) Using the gas fraction probability density function for each cluster, we have produced combined gas fractions for the four detections, for the three non-detections, and for all seven. The Bayesian evidence shows that the first is the correct one to use in the context of trying to measure a low-z global gas fraction. For this, we here find $f_{\rm gas} = 0.08^{+0.06}_{-0.04}\, h^{-1}_{100}$.

(vi) Gas fraction measurement by this SZ-based method is relatively immune from the effect of primordial CMB anisotropy. This is true because the effect on gas mass tends to cancel the effect on total mass on the narrow range of angular scale employed. Simulations show the cancellation to be good for contaminant fluxes of ±50 mJy.

The fact that the analysis method works as well as it does points the way towards analysis of data from upcoming SZ telescopes.

ACKNOWLEDGMENTS

The authors thank the referee for useful comments and suggestions. We thank the staff of Jodrell Bank Observatory, the Mullard Radio Astronomy Observatory and the Teide Observatory for assistance in the day-to-day operation of the VSA. We thank the UK Particle Physics and Astronomy Research Council (PPARC) and the Instituto de Astrofisíca de Canarias for funding and supporting the VSA project. Partial financial support was provided by the Spanish Ministry of Science and Technology, project AYA2001-1657. We thank Angela Taylor for processing and analysing the source-subtractor observations for Coma. We also thank Clive Dickinson, Will Grainger, Charlie McLachlan and Jonathan Zwart for useful discussions. RK thanks Monique Arnaud and Sarah Church for interesting conversations. KL acknowledges support of a PPARC studentship.

REFERENCES

Allen S. W., Schmidt R. W., Fabian A. C., 2001, MNRAS, 328, L37

Allen S., Schmidt R., Fabian A.C., 2002, MNRAS, 334, L11

Allen S. W., Schmidt R. W., Fabian A. C., Ebeling H., 2003, MNRAS, 342, 287

Arnaud M., Pratt G. W., Pointecouteau E., 2004, Mem. Soc. Astron. Ital., 75, 529

Birkinshaw M., 1999, Phys. Rep., 310, 97

Bonamente M., Joy M. K., Carlstrom J. E., Reese E. D., LaRoque S. J., 2004, ApJ, 614, 56

Böhringer H. et al., 2000, ApJS, 129, 435

Carlstrom J. E., Holder G. P., Reese E. D., 2002, ARA&A, 40, 643

Cavaliere A., Fusco-Femiano R., 1976, A&A, 49, 137

Cavaliere A., Fusco-Femiano R., 1978, A&A, 70, 677

Condon J. J., Cotton W. D., Greisen E. W., Yin Q. F., Perley R. A., Taylor G. B., Broderick J. J., 1998, AJ, 115, 1693

Cowles M. K., Carlin B. P., 1996, J. Am. Statistical Assoc., 91, 883

Dickinson C. et al., 2004, MNRAS, 353, 732

Ettori S., Fabian A. C., 1999, MNRAS, 305, 834

Evrard A. E., 1997, MNRAS, 292, 289

Evrard A. E., Metzler C. A., Navarro J. F., 1996, ApJ, 469, 494

Finoguenov A., Reiprich T. H., Böhringer H., 2001, A&A, 368, 749

Gilks W. R., Richardson S., Spiegelhalter D. J., 1996, Markov Chain Monte Carlo in Practice. Chapman and Hall, London

Grainge K. et al., 2003, MNRAS, 341, L23

Grego L., Carlstrom J. E., Reese E. D., Holder G. P., Holzapfel W. L., Joy M. K., Mohr J. J., Patel S., 2001, ApJ, 552, 2

Gregory P. C., Scott W. K., Douglas K., Condon J. J., 1996, ApJS, 103, 427

Herbig T., Lawrence C. R., Readhead A. C. S., Gulkis S., 1995, ApJ, 449, L5

Hobson M. P., Bridle S. L., Lahav O., 2002, MNRAS, 335, 377

Hughes J. P., Gorenstein P., Fabricant D., 1988, ApJ, 329, 82

King I., 1962, AJ, 67, 471

Kneissl R., Jones M. E., Saunders R., Eke V. R., Lasenby A. N., Grainge K., Cotter G., 2001, MNRAS, 328, 783

Lo K. Y., 2002, in ASP Conf. Ser. Vol. 257, AMiBA 2001: High-Z Clusters, Missing Baryons, and CMB Polarization, The Current State of Astronomy in Taiwan and AMiBA. Astron. Soc. Pac., San Francisco, pp. 3+

Markevitch M., Forman W. R., Sarazin C. L., Vikhlinin A., 1998, ApJ, 503, 77

Marshall P. J., Hobson M. P., Slosar A., 2003, MNRAS, 346, 489

Mason B. S., Leitch E. M., Myers S. T., Cartwright J. K., Readhead A. C. S., 1999, AJ, 118, 2908

Mason B. S., Myers S. T., 2000, ApJ, 540, 614

Mason B. S., Myers S. T., Readhead A. C. S., 2001, ApJ, 555, L11

Mohr J. J., Mathiesen B., Evrard A. E., 1999, ApJ, 517, 627

Mohr J. J., Carlstrom J. E., The SZA Collaboration 2002, in ASP Conf. Ser. Vol. 257, AMiBA 2001: High-Z Clusters, Missing Baryons, and CMB Polarization, The SZ-Array: Configuration and Science Prospects. Astron. Soc. Pac., San Francisco, p. 43

Myers S. T., Baker J. E., Readhead A. C. S., Leitch E. M., Herbig T., 1997, ApJ, 485, 1

Ó Ruanaidh J., Fitzgerald W., 1996, Numerical Bayesian Methods Applied to Signal Processing. Springer-Verlag, New York

Peacock J., 1999, Cosmological Physics. Cambridge Univ. Press, Cambridge

Pointecouteau E., Arnaud M., Kaastra J., de Plaa J., 2004, A&A, 423, 33

Pratt G. W., Arnaud M., 2002, A&A, 394, 375

Rebolo R. et al., 2004, MNRAS, 353, 747

Reese E. D., Carlstrom J. E., Joy M., Mohr J. J., Grego L., Holzapfel W. L., 2002, ApJ, 581, 53

Rubiño-Martin J. A. et al., 2003, MNRAS, 341, 1084

Sanderson A. J. R., Ponman T. J., 2003, MNRAS, 345, 1241

Scheuer P. A. G., 1957, Proc. Cam. Phil. Soc., 53, 764

Scott P. F. et al., 2003, MNRAS, 341, 1076

Sivia D., 1996, Data Analysis: A Bayesian Tutorial. Oxford Univ. Press, Oxford

Skilling J., 2002, BayeSys3 manual, unpublished (see http://www.maxent.co.uk)

Slosar A. et al., 2003, MNRAS, 341, L29

Struble M. F., Rood H. J., 1991, ApJS, 77, 363

Sun M., Jones C., Murray S. S., Allen S. W., Fabian A. C., Edge A. C., 2003, ApJ, 587, 619

Sunyaev R. A., Zel'dovich Y. B., 1972, Comm. Astrophys., 4, 173

Taylor A. C. et al., 2003, MNRAS, 341, 1066

Waldram E. M., Pooley G. G., Grainge K. J. B., Jones M. E., Saunders R. D. E., Scott P. F., Taylor A. C., 2003, MNRAS, 342, 915

Watson R. A. et al., 2003, MNRAS, 341, 1057

White S., Navarro J., Evrard A., Frenk C., 1993, Nat, 366, 429

Zhang Y.-Y., Finoguenov A., Böhringer H., Ikebe Y., Matsushita K., Schuecker P., 2004, A&A, 413, 49

This paper has been typeset from a TEX/LATEX file prepared by the author.